

PAPER • OPEN ACCESS

## Low-noise thermal shielding around the cryogenic payloads in the Einstein Telescope

To cite this article: L Busch *et al* 2024 *IOP Conf. Ser.: Mater. Sci. Eng.* **1301** 012013

View the [article online](#) for updates and enhancements.

You may also like

- [Optimization of thermal link for a conduction-cooled superconducting magnet system](#)  
Qing Liang, Chunliu Fang, Xinxin Han et al.
- [Novel technologies and configurations of superconducting magnets for MRI](#)  
Yuri Lvovsky, Ernst Wolfgang Stautner and Tao Zhang
- [The effect of active antennas on the hot-restrike of high intensity discharge lamps](#)  
T Hoebing, A Bergner, B Koch et al.

**PRIME**  
PACIFIC RIM MEETING  
ON ELECTROCHEMICAL  
AND SOLID STATE SCIENCE

**HONOLULU, HI**  
October 6-11, 2024

*Joint International Meeting of*  
The Electrochemical Society of Japan (ECSJ)  
The Korean Electrochemical Society (KECS)  
The Electrochemical Society (ECS)

Early Registration Deadline:  
**September 3, 2024**

**MAKE YOUR PLANS NOW!**

# Low-noise thermal shielding around the cryogenic payloads in the Einstein Telescope

L Busch<sup>1</sup>, G Iaquaniello<sup>2</sup>, P Rosier<sup>2</sup>, M Stamm<sup>3</sup>, and S Grohmann<sup>1,3</sup>

<sup>1</sup>Institute of Technical Thermodynamics and Refrigeration, Organizational Unit: Refrigeration and Cryogenics, Karlsruhe Institute of Technology, 76131 Karlsruhe, Germany

<sup>2</sup>Université Paris-Saclay, CNRS/IN2P3, IJCLab, 91405 Orsay, France

<sup>3</sup>Institute of Beam Physics and Technology, Karlsruhe Institute of Technology, 76344 Eggenstein-Leopoldshafen, Germany

E-mail: lennard.busch@kit.edu

**Abstract.** The Einstein Telescope (ET) is a planned third-generation gravitational-wave detector that includes a low-frequency (LF) and a high-frequency (HF) laser interferometer. Cryogenic operation of ET-LF is imperative for exploiting the full scientific potential of ET, with mirrors operated at temperatures of 10 K to 20 K in order to reduce the thermal noise. Thermal shielding around the optics is essential to support the cooldown process and to decrease the heat load. Additionally in steady-state operation, mechanical vibrations must be kept to an absolute minimum in order to limit noise contributions from scattered light.

We present a cooling concept for a thermal shield surrounding the cryogenic optics of ET-LF, which considers rapid cooldown and low vibration in steady-state operation. During cooldown, cooling tubes enable the flow of supercritical helium, driving the shield temperature decrease by forced convection. For steady-state operation, the shield cooling mechanism is converted to static heat conduction in He-II within the same tubes. A first mechanical model is presented that fulfills the thermal and vibrational requirements. Thermal characteristics of the shield are demonstrated by means of analytical and numerical modeling results. Modal and dynamic analyses are performed to obtain natural frequencies and transfer functions.

## 1. Introduction

The Einstein Telescope (ET) is a European third-generation gravitational-wave (GW) detector currently under development. It combines a cryogenic low-frequency (LF) and a room-temperature high-frequency (HF) laser interferometer. GW detection frequencies of ET lie in the range of 3 Hz to 30 Hz (ET-LF) and 30 Hz to 10 kHz (ET-HF). The sensitivity goals of ET require extremely low noise budgets as stated in [1, 2].

A comprehensive study shows that the cryogenic ET-LF is imperative for exploiting the full scientific potential of ET [3]. Its strain target is on the order of  $10^{-22} \text{ Hz}^{-0.5}$  to  $10^{-24} \text{ Hz}^{-0.5}$ . In order to achieve these demanding goals, a test mass operating temperature between 10 K and 20 K is required. Cryogenic test masses are part of the ET-LF payload, which comprises the lower end of the suspension chain attenuating ambient vibrations. A baseline design for the cryogenic payloads is published in [4]. One of the cooling concepts uses static He-II heat conduction inside a suspension tube. He-II operation is enabled by the cryogenic infrastructure concept described in [5]. ET-LF cryogenic payloads are installed in cryostats, requiring thermal shielding that must be optimized regarding the support of the test mass cooldown via thermal radiation [4], the reduction of heat load on the payload during detector operation as well as low vibrations, particularly in the detection frequency band of  $f = 3 \dots 30 \text{ Hz}$ .

Multiple actively-cooled thermal shields are considered in the ET-LF cryostats [5], whilst moving masses close to the core optics, such as the flow of helium, are potentially problematic. Hence, the concept for the innermost shield relies on static He-II heat extraction, equivalently to the payload cooling concept, providing the quietest possible environment for the payload. The focus of this contribution is on a suitable design for this shield.



## 2. Thermal shielding structure

Figure 1 shows a conceptual ET-LF cryostat design including thermal shielding, following the payload baseline in [4]. The cryostat is able to host interferometer mirrors (test masses) with a diameter of up to 600 mm. A maximum payload diameter of 1.25 m is anticipated, fitting through a bottom access with 1.3 m minimum diameter. Considering the required assembly space based on experience from the Virgo GW detector, the inner shield dimensions are 3.0 m in diameter and 3.8 m in height. Figure 1 schematically depicts two additional thermal shields inside the cryostat, which has a large top flange to connect the upper tower containing the room-temperature suspension chain [2].

The helium cooling system concept for ET-LF foresees active cooling of the two outer thermal shields with supercritical helium flow at 80 K to 50 K and 5 K, respectively. The third shield as innermost screen around the payload is cooled at 2 K via thermal conduction through static He-II, avoiding macroscopic fluid flow. Figure 2 presents the conceptual geometry of this shield.

The He-II cooling concept offers sufficient cooling capacity for both the payload and the inner shield. The potentially quietest form of cooling relates to the unique properties of superfluid helium rather than the 2 K temperature level. Particularly relevant is the exceptionally high thermal conductivity [6], yielding a thermal reservoir to absorb and conduct heat in the quietest (i.e. least dissipative) possible manner.

The basic support structure of the shield in Figure 2 consists of straight (vertical) as well as circular (circumferential) extruded hollow metal profiles, forming an interconnected channel system. Helium supply to the shield can be implemented using thin-wall tubes in combination with bellows attached to vibration isolation systems, similar to the heat link concept in the KAGRA GW detector [7]. Two heat link vibration isolation systems are schematically indicated in Figure 1, connected to the shield top, facing inwards (see also Section 4). The thin-wall helium supply tubes connect the shield cooling interface to a cryogenic supply unit in the vicinity of the cryostat [5]. Figure 2 (View B) shows a schematic interface geometry between such tubes and the inner shield. One interface is placed on each circular header at the bottom and top of the shield frame, constituting the supply and return path during cooldown. Between the header profiles with 10 mm inner diameter, vertical profiles with 5 mm inner diameter are installed. The shield frame is covered with 1 mm thick metal panels, providing good thermal contact. A shield material allowing for small thermal gradients as well as a lightweight design is favorable. Therefore, commercially pure aluminum (Al 1000 series) is foreseen for both the welded frame profiles and the panels. The resulting total shield mass is ca. 450 kg.

## 3. Thermal modelling

The ET-LF inner thermal shield as displayed in Figure 2 has three operating modes: (I) pre-cooling from 300 K to 3 K or 4 K via forced convection heat transfer with a supercritical helium flow, (II) He-II condensation into the pre-cooled shield, and (III) steady-state operation with static He-II heat conduction. While pre-cooling with helium at adjustable temperatures is rather straightforward [5], the latter two modes are explained in the following.

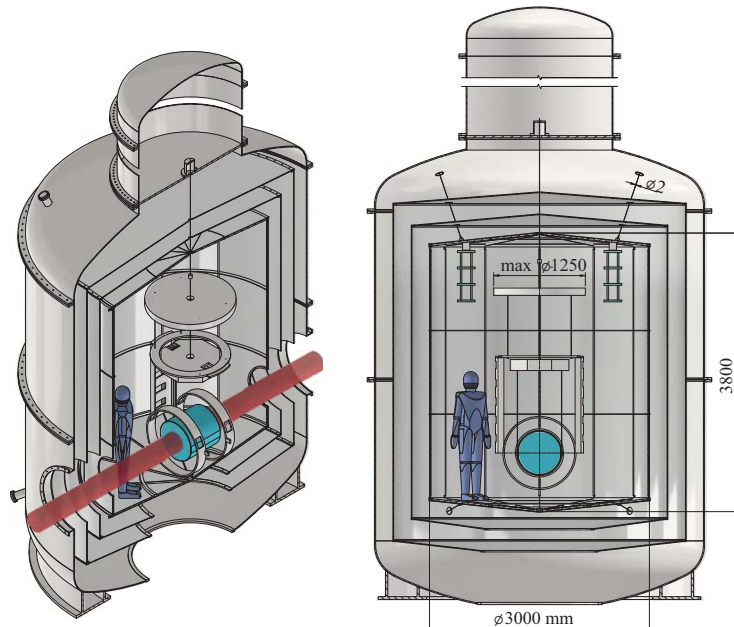


**Figure 1.** Conceptual layout of thermal shields for cryogenic ET-LF payloads within a dummy cryostat including indicated interferometer laser beam.

### 3.1. Steady-state operation

Based on first estimations, we define an engineering design target of  $\dot{Q}_{\text{total}} = 2.0 \text{ W}$  total heat load on the ET-LF inner thermal shield at the steady-state operating temperature  $T_{\text{shield}} \approx 2 \text{ K}$ . Contributions are expected to originate from multiple optical view ports for local payload control [8], from thermal radiation from the beam pipe, from scattered laser light, and from the shield suspensions. Other sources are mitigated by means of the additional active shielding (cf. Figure 1). Based on  $\dot{Q}_{\text{total}}$ , FEM simulations have been conducted. Assuming the shield frame profiles at a uniform temperature of  $T = 1.9 \text{ K}$  and a homogeneous distribution of  $\dot{Q}_{\text{total}}$  on the shield surfaces yields temperature gradients of  $\Delta T_{\text{sh}} < 100 \text{ mK}$ . About  $5/8$  of  $\dot{Q}_{\text{total}}$  is absorbed by the vertical and  $3/8$  by the header frame profiles. The results again can be used to approximate the static 1D temperature profiles within the He-II channels via the differential equation

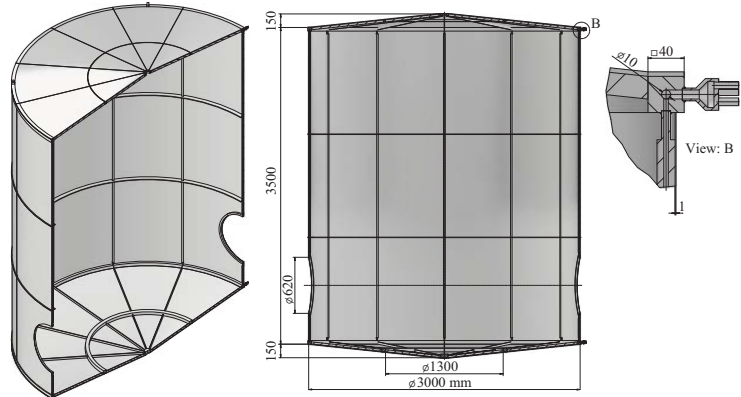


**Figure 2.** Conceptual design of the inner thermal shield in an ET-LF test mass cryostat, cooled with static He-II.

$$\frac{dT}{dx} = \frac{-\dot{q}_{\text{He-II}}(x)^m}{k_{\text{eff}}(T(x), p_r)}, \quad (1)$$

where  $k_{\text{eff}}$  is the empirical thermal conductivity function by Sato et al. [9] with the Gorter-Mellink exponent [10]  $m = 3.4$ , while the channel pressure is denoted by  $p_r$ . The heat flux  $\dot{q}_{\text{He-II}}$  towards the heat sink at  $x = 0$  is approximated to increase linearly. The He-II channels and their interconnections are treated as a fluid column grid, which allows consecutive solving of Equation (1). In each grid segment, the temperature increase in the previous channel section is considered by the value of  $T(x = 0)$ . Exemplary results yield He-II temperatures from 1.85 K at the supply connections to 1.87 K at the farthest point from the He-supply.

### 3.2. He-II condensation into the pre-cooled shield

Subsequent to pre-cooling with supercritical helium flow, the pressure in the shield is reduced to the He-II reservoir pressure  $p_r \approx 1.2 \text{ bar}$  by means of the infrastructure explained in [5] and flow is halted. With a temperature of 3 K to 4 K, the helium is in a sub-cooled liquid state. The last cooldown step then includes the conversion of the normal He-I to the superfluid He-II within the hollow frame profiles. This is achieved by connecting the supply and return lines of the shield *in parallel* to the He-II reservoir, causing the He-II phase front to propagate into the shield by absorbing the sensible heat<sup>1</sup> from both the He-I and the shield, and conducting it to the reservoir via static He-II heat conduction. At  $T_\lambda$ , the superfluid phase forms with dramatic property changes [13, 14].

The following model describes the superfluid phase front propagation, starting from a He-II reservoir at the coordinate  $x = 0$ . Figure 3 visualizes the calculation principles of the one-dimensional model at an intermediate time  $t$ . At the start of the conversion process at  $t = 0 \text{ s}$ , the fluid connection to the He-II reservoir at  $T_r < T_\lambda$  is opened with the cross-sectional area  $A_{\text{He}}$ . All He-I in the channel is at the uniform pre-cooling temperature  $T_{\text{start}} > T_\lambda$  and at the reservoir pressure  $p_r$ . The reservoir temperature  $T_r$  is held constant by the cooling system. In the transient process, the temperature of the He-I next to the phase front is decreased via thermal conduction first to and then below  $T_\lambda$ . Thereby the phase front, characterized by the fixed temperature  $T_\lambda(p_r)$ , successively progresses along the length of the channel that is modeled with an adiabatic end.

<sup>1</sup> The He-I/He-II phase transition is of second order, thus no latent heat is evolved [11]. However, there is a strong increase of heat capacity near the transition temperature  $T_\lambda$  [12].

To consider the synchronous cooldown of the shield, the respective cross-sectional areas  $A_{\text{He}}$  and  $A_{\text{sh}}$  are included in the model, assuming ideal solid-to-liquid heat transfer.

The He-II condensation model is divided into two parts. The first part describes the movement of the phase front position  $x_\lambda(t)$  along the channel length by differential equations, while the second part introduces a numerical approximation of the He-I region to obtain complete temperature profiles of the cooldown process. In the region  $T < T_\lambda$  left of the phase front in Figure 3, static He-II heat conduction dominates the heat transport from the He-I phase and the surrounding thermal mass due to the extremely high thermal conductivity of He-II. Therefore, the heat flux  $\dot{q}$  from the phase front at  $(T_\lambda, x_\lambda)$  to the reservoir at  $(T_r, 0)$  is given by

$$\dot{q}(x_\lambda) = \left[ \frac{1}{x_\lambda} \int_{T_\lambda}^{T_r} k_{\text{eff}}(T, p_r) dT \right]^{\frac{1}{m}}. \quad (2)$$

The enthalpy change of an infinitesimally short element  $dx$  to the right of the phase front due to the temperature change from  $T_{\text{start}}$  to  $T_\lambda$  is

$$dH_\lambda = dx \int_{T_{\text{start}}}^{T_\lambda} [A_{\text{He}} \rho_{\text{He-I}}(T, p_r) c_{p, \text{He-I}}(T, p_r) + A_{\text{sh}} \rho_{\text{sh}} c_{\text{sh}}(T)] dT, \quad (3)$$

where  $\rho$  and  $c$  denote density and specific heat capacity, and  $A_{\text{sh}}$  is the cross-sectional area of the adjacent shield mass homogeneously distributed along the channel length  $L_{\text{channel}}$ . The time derivative of the enthalpy change in the element equals the heat flow through the He-II region

$$\frac{dH_\lambda}{dt} = \dot{q}(x_\lambda) A_{\text{He}}. \quad (4)$$

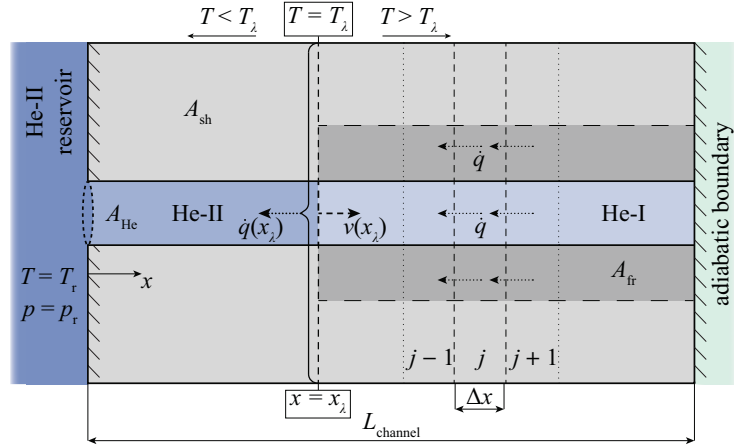
The combination of Equations (3) and (4) yields the velocity of the phase front propagating from the reservoir into the He-I region

$$v(x_\lambda) = \frac{dx_\lambda}{dt} = \frac{A_{\text{He}} \dot{q}(x_\lambda)}{\int_{T_{\text{start}}}^{T_\lambda} [A_{\text{He}} \rho_{\text{He-I}}(T, p_r) c_{p, \text{He-I}}(T, p_r) + A_{\text{sh}} \rho_{\text{sh}} c_{\text{sh}}(T)] dT}, \quad (5)$$

with  $\dot{q}(x_\lambda)$  from Equation (2). Hence, the time relation for the He-II phase front position is

$$t(x_\lambda) = \int_0^{x_\lambda} \frac{1}{v(x)} dx \quad \text{with} \quad t(0) = 0. \quad (6)$$

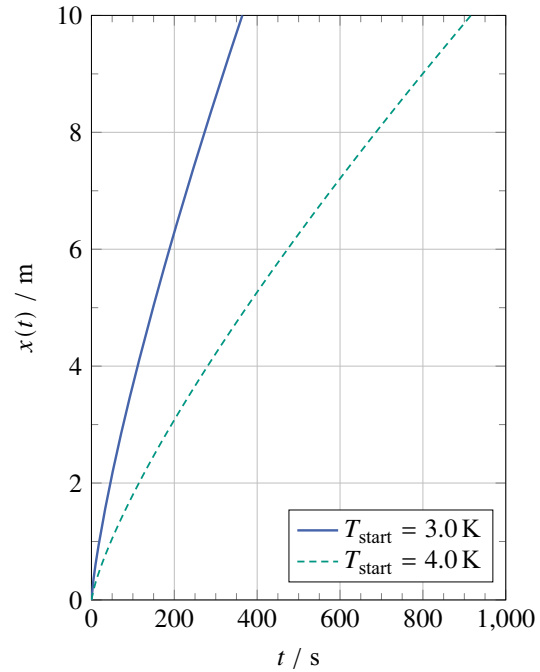
Figure 4 shows the phase front positions calculated with the system parameters and material properties listed in Table 1.  $A_{\text{He}}$  and  $A_{\text{sh}}$  are chosen considering the internal diameter of the hollow frame profiles as well as the approximate shield mass distribution comprising both frame and panels (cf. Figure 2). At the pre-cooling temperature of 3.0 K as planned in [5], the phase front reaches a 10 m far end of the channel after  $t \approx 360$  s. In this period of time, an amount of heat of around 260 J is removed from the shield section, including the helium column. Simultaneously, around 180 J are deposited due to  $\dot{Q}_{\text{total}}$ . This allows a rough estimation of  $t > 600$  s



**Figure 3.** Scheme of the 1D semi-analytical superfluid phase front movement model for a circular helium channel surrounded by the thermal mass of the shield and the shield frame, respectively.

**Table 1.** Parameters and material property references used in the He-II condensation model.

Parameter/property	Value/reference
$T_{\text{start}}$	3.0 ... 4.0 K
$T_r$	1.85 K
$p_r$	1.2 bar(a) [5]
$L_{\text{channel}}$	10 m
$A_{\text{He}}$	78.5 mm <sup>2</sup>
$A_{\text{sh}}$	6830 mm <sup>2</sup>
$(\rho, c_p)_{\text{He-I}}$	HEPAK [15, 16]
$k_{\text{He-I}}$	REFPROP [17]
$T_\lambda(p_r)$	2.166 K [15, 16]
$k_{\text{eff}}$	Sato et al. [9]
$c_{\text{Al}}^1$	Kittel [18]
$k_{\text{Al1000}}^2$	Hartmann et al. [19]
	Woodcraft et al. [20]
$A_{\text{fr}}$	1520 mm <sup>2</sup>
$\Delta x$	1 mm
$\Delta t$	1 ms

<sup>1</sup> Including phonon [18] and electron [19] contributions.<sup>2</sup> Al 1000 series – lower limit [20].**Figure 4.** Superfluid phase front position in an aluminum channel as a function of time.

for the completion of the He-II condensation process along  $L_{\text{channel}}$ . If pre-cooling is provided only at 4.0 K, the mean phase front velocity is about 2.5 times lower. Compared to the cryogenic payload cooldown taking several days [4], the He-II phase front propagation is fast and not a limiting parameter. The propagation results are in good agreement with Bielert et al. [21], using the parameters  $A_{\text{sh}} = 0 \text{ m}^2$ ,  $T_r = 1.9 \text{ K}$  and  $T_{\text{start}} = 4.5 \text{ K}$  at saturation pressure  $p_r \approx 1.3 \text{ bar}$  in the model. Relative deviations  $< 5 \%$  originate from the updated  $k_{\text{eff}}$  model as well as the Gorter-Mellink coefficient.

In order to calculate the temperature profile along the He-II region for every value of  $x_\lambda$ , Equation (1) is solved in the interval  $x = 0 \dots x_\lambda$  with  $T(x = 0) = T_r$ . To determine the temperature profile to the right of the phase front at  $T > T_\lambda$ , thermal conduction through the cross-section of the channel frame  $A_{\text{fr}}$  cannot be neglected, because  $k_{\text{He-I}} < k_{\text{Al1000}} \ll k_{\text{eff}}$  and  $A_{\text{He}} < A_{\text{fr}}$ . Modelling of heat transfer in this region is implemented by means of a Crank-Nicolson implicit numerical scheme [22]. The region is discretized into elements of length  $\Delta x$ , yielding a total number of  $N = L_{\text{channel}}/\Delta x$  elements at  $t = 0 \text{ s}$ . The Crank-Nicolson scheme comprises a three-point stencil. Thus, heat flows to/from an element  $j$  are considered from/to its adjacent cells  $j - 1$  and  $j + 1$  as indicated in Figure 3. The governing equation of energy change and 1D Fourier heat conduction is

$$\left[ A_{\text{He}} \rho_{\text{He-I}}(T, p_r) c_{p, \text{He-I}}(T, p_r) + A_{\text{sh}} \rho_{\text{sh}} c_{\text{sh}}(T) \right] \frac{\partial T}{\partial t} = \frac{\partial}{\partial x} \left[ A_{\text{fr}} k_{\text{fr}}(T) + A_{\text{He}} k_{\text{He-I}}(T, p_r) \right] \frac{\partial T}{\partial x}, \quad (7)$$

which is evaluated numerically. The superfluid phase front propagation is implemented by means of a moving boundary condition via the results for  $x_\lambda(t)$  presented above. This yields a progressive decrease of  $N$  over time with a temperature of  $T_{j=0} = T_\lambda$  in the first cell.

The complete temperature profiles  $T_{\text{He}}(x, t)$  along the channel are obtained by combining the results for the He-II and He-I regions calculated at discrete time steps  $t = i \cdot \Delta t$  with  $i \in [1.. \lfloor t(L_{\text{channel}})/\Delta t \rfloor]$ . Figure 5 shows the evolution of such temperature profiles. The complete temperature gradient in the He-I region,  $T_{\text{start}} - T_\lambda \approx 0.83 \text{ K}$ , occurs within around 10 mm next to the phase front. Temperature gradients in the He-II phase are small and decrease continuously as the phase front propagates. Increased gradients are only observed close to the phase front, where  $k_{\text{eff}}$  decreases strongly towards  $T_\lambda$  starting from the peak value around 1.9 K. Following the steep temperature gradients of the displayed curves, a slight reduction of the phase front velocity

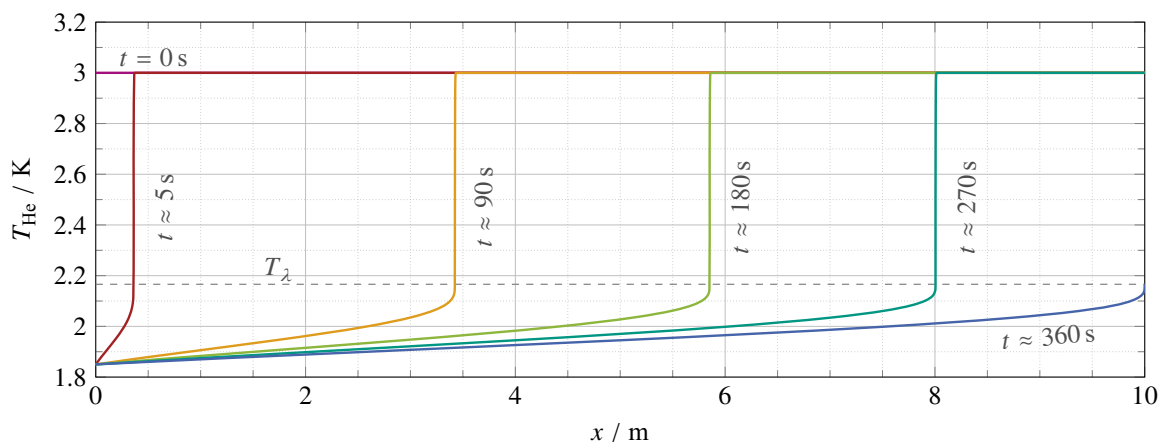


**Figure 5.** Temperature gradients along a 1D helium channel for the parameters in Table 1 at  $T_{\text{start}} = 3.0$  K.

over time can be recognized (shorter distances at equivalent time intervals).

#### 4. Modal analyses

Given low-noise cooling as described in the previous sections, an adequate mechanical shield design must reduce otherwise significant detector noise contributions. One of the two main contributions is caused by back-scattering of light from all surfaces with a viewing angle to the mirror [23]. The other is induced by mechanical coupling between the attachment point of a payload heat link vibration isolation system and the payload itself [24]. In order to account for these contributions, two major shield vibration mitigation aspects are considered from the early stages of the shield design on: (I) reduction of the vibrational transfer function from the ambiance to the shield and (II) elevation of the structural resonant frequencies of the shield (i.e. box modes).

The former aspect, yet in prospect, is indicated in Figure 1. The approach is to suspend the shield via maraging steel wires through magnetic damping systems located within attachments to the cryostat lid. Additional wires at the bottom side of the shield enable reducing displacement of this extremity in order to constrain the pendulum mode frequencies.

Regarding aspect (II), the shield needs to comprise sufficient structural reinforcements (cf. Figure 2) at limited total weight so as not to spoil the suspension- and cooldown performances. In a first phase, the design of the shield has been evaluated in terms of structural, modal and dynamical characteristics, with iterative improvements on decisive geometrical parameters such as panel and frame thickness, structural shape and additional ribs. For a finite element analysis, mechanical material properties were taken from [25]. In terms of vibration and sensitivity to seismic activities as well as ambient instrumentation and equipment noise, first, the natural frequencies in free modal analysis were investigated and increased to avoid low frequency resonance in the range below 30 Hz, i.e. within the ET-LF detection frequency band. As Figure 6a shows, preliminary results yield improved natural frequencies of ca. 45 Hz for the shield faces at ca. 51.5 Hz for the shell. This opposes to ca. 4 Hz for an unreinforced structure.

Subsequently, transfer functions in frequency harmonic response were calculated to estimate the resulting shield deformation amplitudes at these specific resonant frequencies. The spatially resolved vibrational amplitude results further allow locating favorable, low-noise attachment positions of the payload heat link vibration isolation system (cf. Figure 1) and estimating the respective vibration source constraints.

The frequency response analysis was conducted in the frequency range  $f = 0$  Hz...53 Hz using the spatial shield discretisation indicated in Figure 6a with a conservative structural damping ratio of 2 %. Figure 6b shows respective results at the nodes exhibiting the maximum displacement values in longitudinal and transversal directions, with magnitudes of ca. 31 near the center of the shield faces at  $f \approx 45$  Hz, and ca. 16 in the center of the shell panels at  $f \approx 51.5$  Hz. Furthermore, it is indicated that the dynamic response of the pursued shield structure minimizes the risk of vibration within the ET-LF detection frequency band. Below 30 Hz, the amplification magnitudes stay at a low level, to be compared with the interferometer noise budget requirements.

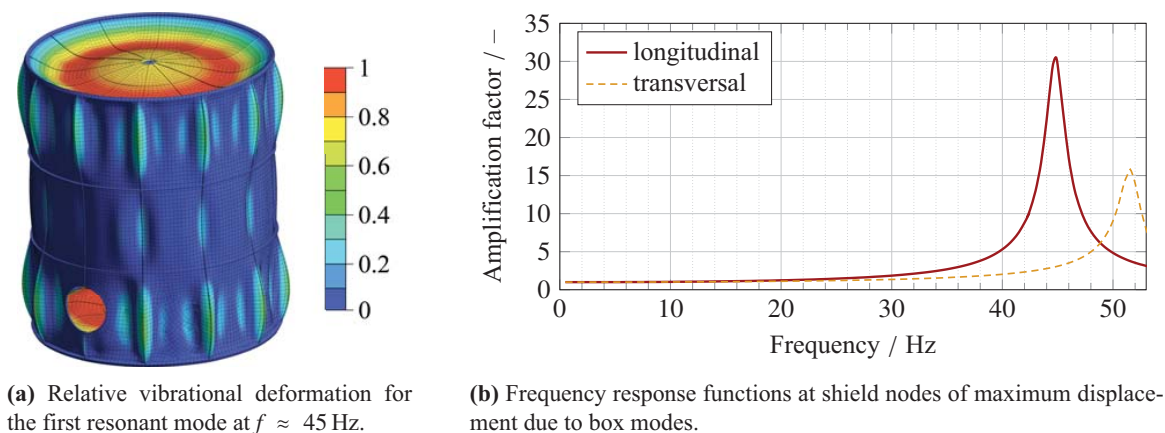


**Figure 6.** Modal and harmonic response analysis results.

## 5. Conclusions and prospects

A low-noise inner thermal shielding for the ET-LF cryostats based on static He-II cooling is presented. The shield frame comprises extruded aluminum profiles for cooldown with supercritical helium flow, and for steady-state operation with static He-II heat conduction. The condensation of He-II into the pre-cooled shield is modeled by differential equations, demonstrating the overall feasibility and showing that the phase front propagation driven only by the He-II heat conduction is sufficiently fast. The modeling of the steady-state thermal behavior shows temperature gradients in the shield below 100 mK.

Further, the results of an iterative process of shield structure alteration show significantly improved shield resonant frequency modes and quantify the vibration amplitudes with transfer functions in frequency harmonic response. These results are required to understand and conduct a noise evaluation due to light back-scattering into the mirror. This structural shield concept paves the way to investigate in further detail the support of the shield through magnetically damped wire suspensions.

Finally, this development will serve as decisive input for the study of payload heat link vibration isolation systems. Within the He-II cooling concept for ET-LF, the heat links are foreseen to be thin tubes with bellows enabling helium supply. Similar tubes are envisaged to supply the presented ET-LF inner shield. Tangible plans for future experimental work on the detailed design and implementation of these interfaces in the Einstein Telescope exist.

## 6. References

- [1] Hild S *et al*, 2011 *Class Quantum Gravity* **28(9)** 094013
- [2] ET Steering Committee Editorial Team, 2020 Design Report Update for the Einstein Telescope. Tech. Rep. ET-0007B-20
- [3] Branchesi M *et al*, 2023 *JCAP* **2023(07)** 068
- [4] Korovesi X, Busch L, Majorana E, Puppo P, Rapagnani P, Ricci F, Ruggi P and Grohmann S, 2023. Cryogenic payloads for the Einstein Telescope - Baseline design with heat extraction, suspension thermal noise modelling and sensitivity analyses. (arXiv:2305.01419 [astro-ph.IM])
- [5] Busch L and Grohmann S, 2022 *IOP Conf. Ser.: Mater. Sci. Eng.* **1240(1)** 012095
- [6] Van Sciver S W, 2012 *Helium Cryogenics* (Springer, New York, NY)
- [7] Yamada T on behalf of the KAGRA Collaboration, 2020 *JPCS* **1468(1)** 012217
- [8] The Virgo Collaboration, 2012 Advanced Virgo Technical Design Report. Tech. Rep. VIR-0128A-12, European Gravitational Observatory (EGO)
- [9] Sato A, Maeda M, Dantsuka T, Yuyama M and Kamioka Y, 2006 *AIP Conf. Proc.* **823(1)** 387–392

- [10] Gorter C J and Mellink J, 1949 *Physica* **15** 285–304
- [11] Ehrenfest P, 1933 In *Proc. Royal Acad. Amsterdam*. vol. 36, 153–157 (Commun. Kamerlingh Onnes Inst. Leiden, Suppl. 75b)
- [12] Keesom W and Clusius K, 1932 In *Proc. Royal Acad. Amsterdam*. vol. 35, 307 (Commun. Kamerlingh Onnes Inst. Leiden, Suppl. 219e)
- [13] Tisza L, 1938 *Nature* **141** 913
- [14] Landau L, 1941 *Phys. Rev.* **60(4)** 356–358
- [15] Horizon Technologies, CryoData Inc, 1998. HEPAK™ Version 3.4. Littleton, CO
- [16] Arp V D, McCarty R D and Friend D G, 1998 Thermophysical properties of Helium-4 from 0.8 to 1500 K with pressures to 2000 MPa. Tech. Rep. 1334 (revised), National Institute of Standards and Technology
- [17] Lemmon E W, Bell I H, Huber M L and McLinden M O, 2018. NIST Standard Reference Database 23: Reference Fluid Thermodynamic and Transport Properties-REFPROP, Version 10.0, National Institute of Standards and Technology
- [18] Kittel C, 2018 *Introduction to Solid State Physics* (John Wiley & Sons, Hoboken)
- [19] Hartmann W M, Culbert H V and Huebener R P, 1970 *Phys. Rev. B* **1(4)** 1486–1493
- [20] Woodcraft A L, 2005 *Cryogenics* **45(9)** 626–636
- [21] Bielert E R, Verweij A P and Ten Kate H H J, 2013 *Cryogenics* **53** 78–85
- [22] Crank J and Nicolson P, 1947 *Math. Proc. Camb. Phil. Soc.* **43(1)** 50–67
- [23] Fritschel P and Yamamoto H, 2013 Scattered light noise due to the ETM coating ripple. Technical Note LIGO-T1300354-v3, LIGO Scientific Collaboration
- [24] Bajpai R, Tomaru T, Kimura N, Ushiba T, Yamamoto K, Suzuki T and Honda T, 2022 *Classical and Quantum Gravity* **39(16)** 165004
- [25] Schwartzberg F R, Knight M, Martin Marietta Corporation and Air Force Materials Laboratory (US), 1970 Technical Documentary Report. No. 1 in *Cryogenic Materials Data Handbook* (National Technical Information Service, Springfield, VA)

### Acknowledgments

The authors would like to acknowledge the support from the German Ministry for Education and Research (BMBF, Gr 05A20VK4), and from the Karlsruhe School of Elementary Particle and Astroparticle Physics: Science and Technology (KSETA).